Acta Pharmaceutica Sinica B 2026;16(4):2570−2586

Chinese Pharmaceutical Association
Institute of Materia Medica, Chinese Academy of Medical Sciences

Acta Pharmaceutica Sinica B

www.elsevier.com/locate/apsb
www.sciencedirect.com

ORIGINAL ARTICLE

A spatiotemporal selective bioinspired hybrid system engineered for preventing post-thrombolysis recurrence by inhibiting the ferroptosis pathway and reprogramming macrophages

Tianjiao Hao[a,†], Bin Gao[b,†], Yuanyuan Zhou[a], Chang Liu[c], Chuanjiang Ran[a], Binghua Chang[a], Wei You[d], Qiyue Wang[e,*], Jun Ye[f,g,*], Yan Shen[a,*]

[a]*Department of Pharmaceutics, State Key Laboratory of Natural Medicines, School of Pharmacy, China Pharmaceutical University, Nanjing 211198, China*
[b]*Department of Internal Medicine, Taixing Chinese Medicine Hospital, Taixing 225400, China*
[c]*National Engineering Research Center for Gelatin-based Traditional Chinese Medicine, Liaocheng 252201, China*
[d]*Department of Cardiology, Nanjing First Hospital, China Pharmaceutical University, Nanjing 210006, China*
[e]*School of Pharmaceutical Science, Nanjing Tech University, Nanjing 211816, China*
[f]*State Key Laboratory of Bioactive Substance and Function of Natural Medicines, Institute of Materia Medica, Chinese Academy of Medical Sciences & Peking Union Medical, Beijing 100730, China*
[g]*Beijing Key Laboratory of Key Technologies for Natural Drug Delivery and Novel Formulations, Beijing 100730, China*

Received 6 May 2025; received in revised form 15 August 2025; accepted 4 September 2025

KEY WORDS

Thrombus;
Biomimetic hybrid nanocarriers;
Thrombus microenvironment

Abstract Cardiovascular diseases induced by arterial thrombosis, such as myocardial infarction and ischemic stroke, have gradually emerged as critical threats to human life and health. Sequentially targeted delivery systems are highly desired to be developed to improve the delivery of thrombolytics and anti-inflammatory medications to the site of the thrombus, respectively, to pursue a maximized combinational effect. Herein, we developed a probiotic-platelet hybrid vesicle-targeted drug delivery system (Fer-1@PLevs-C&U) to achieve sequential anti-thrombolytic delivery against thrombus and prevent its recurrence. The hybrid vesicles (PLevs) were prepared by mixing platelet membrane with

*Corresponding authors.
E-mail addresses: qiyue.wang@njtech.edu.cn (Qiyue Wang), yelinghao@imm.ac.cn (Jun Ye), shenyan@cpu.edu.cn (Yan Shen).
†These authors made equal contributions to this work.

Peer review under the responsibility of Chinese Pharmaceutical Association and Institute of Materia Medica, Chinese Academy of Medical Sciences.

https://doi.org/10.1016/j.apsb.2026.01.014
2211-3835 © 2026 The Authors. Published by Elsevier B.V. on behalf of Chinese Pharmaceutical Association and Institute of Materia Medica, Chinese Academy of Medical Sciences. This is an open access article under the CC BY-NC-ND license (http://creativecommons.org/licenses/by-nc-nd/4.0/).

improvement;
Efficient thrombolysis;
Multiple covalent targeting system;
Macrophages regulation;
Ferroptosis;
Post-thrombolysis recurrence

Lactobacillus plantarum-derived bacterial extracellular vesicles (Levs) and further decorated with DSPE-PEG_{2000}-CREKA, achieving "point-to-point" multi-covalent targeting of thrombus components. After targeted localization to the arterial thrombotic site, Fer-1@PLevs-C&U gradually releases the thrombolytic drug urokinase-type plasminogen activator (UPA) and Ferroptosis inhibitor (Fer-1) to facilitate thrombus dissolution and regulate the inflammatory microenvironment. By enhancing the eNOS expression and reducing the secretion of inflammatory factors TNF-α and IL-6, Fer-1@PLevs-C&U significantly reduced the inflammatory microenvironment and inhibited recurrent thrombus. Therefore, Fer-1@PLevs-C&U constitutes a novel biomimetic drug delivery platform with promising therapeutic potential and practical applicability.

© 2026 The Authors. Published by Elsevier B.V. on behalf of Chinese Pharmaceutical Association and Institute of Materia Medica, Chinese Academy of Medical Sciences. This is an open access article under the CC BY-NC-ND license (http://creativecommons.org/licenses/by-nc-nd/4.0/).

1. Introduction

The mortality rate from cardiovascular disease continues to rise[1], with ischemic heart disease and ischemic stroke accounting much of the total global deaths from cardiovascular disease, becoming the leading causes of cardiovascular disease[2,3]. Thrombosis is mainly composed of platelet aggregates bound together by fibrin chains. In the inflammatory microenvironment at the site of arterial thrombosis, vascular inflammation produces a large amount of reactive oxygen species (ROS) in the vascular wall, a key factor causing endothelial dysfunction, which in turn mediates the increase of proinflammatory cytokines and chemokines[4−6], as well as the activation and adhesion of white blood cells to the vascular wall, leading to the stable formation of arterial thrombosis[7−9]. Therefore, improving the microenvironment of thrombotic inflammation is significant for treating thrombosis and preventing its recurrence. However, oral delivery medicines face problems such as poor targeting ability, short *in vivo* circulation time, and cell barrier penetration[10,11], limiting their application in anti-thrombus treatment. Optimizing drug delivery system design to reduce off-target and side effects remains a significant challenge to ensure safe, sustainable, and accurate drug delivery *in vivo*.

A successful drug delivery system could comprehensively regulate the drug biodistribution in terms of space, time, and dosage. The key improvement in therapeutic efficacy of the formulations is to deliver the appropriate amount of drug to the correct disease location at the appropriate time, thereby achieving the expected drug release. Spatiotemporally selective drug delivery systems have been considered one of the most effective therapeutic strategies for regulating thrombus formation. The pre-thrombotic phase, characterized by endothelial cell dysfunction and substantial deposition of inflammatory macrophages beneath the endothelium, facilitates the binding of platelets to the endothelium through GPIb−IX−V complexes on the surface of platelets[12−16]. In a receptor-ligand coupling process, this results in endothelial cell chemotactic adhesion. Membrane proteins on the platelet surface, present in platelet membranes from mice, mediate endothelial cell tropism and exhibit natural endothelial-targeting properties that promote thrombus homing[17−19]. Secondly, the specific uptake of probiotic vesicles by inflammatory macrophages enables targeting these cells at the thrombus site[20−22]. Lastly, by combining the fibrin-targeting property of the CREKA peptide with the physical coupling of the peptide to hybridized vesicles through lipid insertion, thrombus fibrin can be targeted to enhance the penetration of nanocarriers in the fibrin network[23−26]. Reasonable design of the nanocarrier utilizing the above elements allows for the subsequent release of thrombolytic drugs, with the help of multiple covalently targeted nanocarriers, reducing the risk of untargeted activation of the systemic thrombolytic system and improving thrombolytic efficacy at the thrombus site.

Accordingly, Ferrostatin-1 (Fer-1) is gradually released from the nanocarriers at the target site, resulting in a synergistic anti-inflammatory effect in combination with the probiotic vesicle (Levs). This synergy reduces intracellular reactive oxygen species (ROS) and proinflammatory cytokines, while also promoting the polarization of macrophages from the proinflammatory M1 phenotype to the anti-inflammatory M2 phenotype[27−29]. Ultimately, this combined anti-inflammation action helps to alleviate oxidative stress in the microenvironment and reduce endothelial cell damage and persistent thrombus generation caused by chronic inflammation[30−34]. Additionally, the expression of endothelial nitric oxide synthase (eNOS) is increased[35], further improving endothelial function and achieving the goal of enhancing the thrombosis microenvironment and reducing the likelihood of thrombus recurrence[36−39].

Based on the biological characteristics of platelet aggregation, fibrin network formation, and the recruitment of inflammatory cells at thrombus sites, this study designed a probiotic-platelet hybrid vesicle-targeted drug delivery system for the spatiotemporally selective co-delivery of Fer-1 and UPA (Fer-1@PLevs-C&U). The hybrid PLevs were prepared by extruding the platelet membrane and the extracellular vesicle (Levs) of Lactobacillus WCFS1, followed by physically coupling the fibrin-targeting peptide DSPE-PEG_{2000}-CREKA through lipid insertion to achieve "point-to-point" multiple covalent targeting of thrombus components. Subsequently, the hybrid vesicle was sequentially co-incubated with the ferroptosis inhibitor Fer-1 and externally coupled with the UPA through surface modification to complete the construction of the final drug-loaded hybrid vesicle delivery vehicle (Fer-1@PLevs-C&U), aiming to achieve efficient and precise thrombolysis as well as improve the thrombotic microenvironment. Fer-1@PLevs-C&U could be distributed to the thrombotic area by the platelet membrane-based thrombosis targeting and UPA release. Subsequently, the bacterial extracellular vesicle component in the carrier induced macrophage identification and phagocytosis, further releasing Fer-1 against ferroptosis-induced inflammation in the thrombotic area. Moreover, the Fer-1@PLevs-C&U could also significantly reduce the inflammatory microenvironment and inhibit recurrent thrombus, suggesting a potential anti-thrombus nanomedicine.

2. Materials and methods

2.1. Materials

Fer-1 was purchased from MedMol (Shanghai, China). UPA was purchased from Macklin Co., Ltd. (Shanghai, China). *Lactobacillus plantarum* WCFS1 was obtained from Nanjing Normal University (Nanjing, China). Prostaglandin E1 (PGE1) was purchased from Aladdin Biochemical Technology Co., Ltd. (Shanghai, China). *Lactobacilli* MRS Broth and *Lactobacilli* MRS Agar were purchased from Haibo Biopharmaceutical Co., Ltd. (Qingdao, China). DSPE-PEG_{2000} was purchased from AVT (Shanghai) Pharmaceutical Technology Co., Ltd. (Shanghai, China). DSPE-PEG_{2000}-CREKA was purchased from Tanshtech Co., Ltd. (Guangzhou, China). Sulfo-*N*-succinimidyl 4-(maleimidomethyl) cyclohexane-1-carboxylate (Sulfo-SMCC) was purchased from TCI Chemical Industry Development Co., Ltd. (Shanghai, China). The total sulfhydryl content determination kit and lipopolysaccharide (LPS) were purchased from Beijing Solarbio Science & Technology Co., Ltd. (Beijing, China). BCA protein concentration assay kit, reactive oxygen species (ROS) assay kit, TCEP, and Traut's reagent were purchased from Beyotime Biotechnology Co., Ltd. (Shanghai, China). GPVI Antibody (H-5) and CD42b Antibody (E−8) were purchased from Santa Cruz Biotechnology. HUVEC, RAW264.7 cells, Dulbecco's modified Eagle's medium (DMEM), DiR, and DAPI were purchased from Jiangsu KeyGEN BioTECH Co., Ltd. (Nanjing, China). Fetal bovine serum (FBS, No. FBS01) was purchased from Sino Biological (Beijing, China). Rabbit anti-eNOS (AF0096), Rabbit anti-TNF-α (AF7014), Rabbit anti-IL-10 (DF6894), and Rabbit anti-IL-6 (DF6087) were purchased from Affinity Biosciences. (Changzhou, China).

2.2. Preparation of Fer-1@PLevs-C&U

2.2.1. Preparation of Fer-1@PLevs

The platelets were purified using gradient centrifugation. In brief, fresh arterial blood was preserved in anti-coagulant tubes containing potassium citrate (1:9). Then, the whole blood was centrifuged at 200×*g* for 10 min and further centrifuged at 800×*g* for 20 min to obtain platelets. Platelets were subjected to three freeze-thaw cycles and washed three times to get the platelet membrane, which was resuspended in pre-chilled cocktail buffer (0.1 mol/L PBS, 2 mmol/L EDTA, 6−10 mol/L PGE1) for further use.

Lactobacillus plantarum WCFS1 bacterial cells were grown in MRS broth for 24 h at 37 °C. Bacterial cells were removed from the culture broth by centrifugation at 10,000×*g* for 10 min at 4 °C. The supernatants were filtered using a 0.45 μm pore filter (Millipore) and concentrated using an Amicon Ultra filter unit with a MWCO of 100 kDa to remove proteins and other molecules. After that, the supernatants were ultra-centrifuged (150,000×*g* at 4 °C for 2 h) to obtain the probiotic vesicles (Levs). The pellets were then dissolved in PBS, aliquoted, and stored at −80 °C.

The freeze-dried platelet membrane and probiotic vesicles (Levs) were separately reconstituted using PBS, and the protein content of the platelet membrane (M_{PM}) and internal protein content of Levs (M_{Levs}) were determined using the BCA assay. Subsequently, the platelet membrane suspension was uniformly mixed with powdered DSPE-PEG_{2000} at a mass ratio of $M_{DSPE\text{-}PEG2000}$:M_{PM} = 4:1 and sonicated for 5 min to obtain platelet membrane vesicles (PMV). The hybrid vesicles (PLevs) were prepared by uniformly mixing Levs and PMV at a mass ratio of M_{Levs}:M_{PM} = 1:10 under a horizontal shaker (HUAMEI INSTRUMENT, THZ-98, China) at 37 °C (100 rpm, 30 min), followed by being extruded through carbonate membranes (pore size 400 nm and 200 nm, respectively, seven times each).

The Fer-1-loaded hybrid vesicles (Fer-1@PLevs) were prepared by mixing Fer-1 with PLevs under a horizontal shaker at 37 °C (100 rpm, 2 h) at a mass ratio of $M_{Fer\text{-}1}$:M_{PM} = 1:5. The mixture was centrifuged to remove unloaded drugs, and Fer-1@Plevs were collected for further use.

2.2.2. Preparation of Fer-1@PLevs-U and Fer-1@PLevs-C&U

1 mg of Urokinase-type plasminogen activator (UPA) was dissolved in physiological saline (0.4 mol/L HEPES, pH 7.4) to adjust the osmotic pressure to 550 mmol/L, ensuring a pH of 7.4 in the system. Sulfo-SMCC was added dropwise to the UPA buffer at a molar ratio of 1:10, and Tween 80 (0.02%, *w/v*) was added to the reaction system. The reaction was allowed to proceed at 4 °C under a nitrogen atmosphere, and the UPA-SMCC was collected by ultrafiltrating the reaction solution in a 10 kDa ultrafiltration tube at 4000×*g* for 30 min. Freshly prepared Fer-1@PLevs were mixed with 2-iminothiolane hydrochloride (Traut's reagent, 1.0 mg/mL) and stirred at 200 rpm at 4 °C for 1 h. After centrifuging and washing with PBS, the Fer-1@PLevs-SH were mixed with UPA-SMCC and stirred at 200 rpm for 3 h at 4 °C to prepare Fer-1@PLevs-U. In addition, 0.25 mg of DSPE-PEG_{2000}-CREKA was incubated with Fer-1@PLevs-U for 30 min at 37 °C to obtain Fer-1@PLevs-C&U.

2.3. Characterization

2.3.1. Physicochemical property

The particle size and zeta potential of Fer-1@PLevs-C&U were investigated with a Zetasizer Nano-ZS90 (Malvern Instruments, UK). The morphology was characterized by transmission electron microscopy (TEM, HT7700, Hitachi, Japan) after being stained with 1% (*w/v*) phosphotungstic acid. The drug-loading rate of UPA and Fer-1 was measured by the UPA ELISA assay kit and high-performance liquid chromatography (HPLC) (Shimadzu, Japan) (Xtimate® 250 mm × 4.6 mm Welch C18 RP-C18 column, acetonitrile: aqueous solution with formic acid (0.05%) (50:50) as mobile phase, UV wavelength of 254 nm, flow rate of 1 mL/min, column temperature of 35 °C), respectively. The reaction efficiency of UPA-SMCC with UPA was determined using the total sulfhydryl content determination kit.

2.3.2. Physical stability

Freshly prepared Fer-1@PLevs-C&U was stored at 4 °C for one week, with samples taken on Days 0, 1, 3, 5, and 7. The particle size and zeta potential were measured to investigate their stability over the seven days of storage.

2.3.3. Western blot

Freshly prepared solutions of Platelet (PLT), PMV, Fer-1@PLevs, Fer-1@PLevs-U, and Fer-1@PLevs-C&U were lysed with the RIPA buffer, and total protein was collected. The proteins were separated by SDS-PAGE, transferred into a PVDF membrane, and incubated with GPVI and GPIb-α primary antibodies at 4 °C overnight. The membrane was then washed with TBST and incubated with secondary antibodies for 1 h at room temperature. The binding of targeted proteins was imaged using a gel image system (TANON EPS-300).

2.4. Membrane fusion assay

The membrane fusion was evaluated using the Förster fluorescence resonance energy transfer (FRET) assay. One μL of Dil (10 μmol/L) and 2 μL of DiO (5 μmol/L, Beijing Lablead Inc.) were added to the incubation with Levs for 30 min. Dye-containing Levs were mixed with PMV at a mass ratio of 1:10, 1:15, and 1:20, respectively, to prepare Plevs following the process described above. The fluorescence spectra were monitored from 480 to 600 nm, and the fluorescence values were recorded using a microplate reader.

In addition, the membrane fusion was further evaluated by confocal microscopy. PMV and Levs were stained with DiO or Dil, respectively. DiO@PMV and Dil@Levs were sonicated and extruded at a protein ratio of 10:1 to obtain dye-containing hybrid vesicles (DiO&Dil@PLevs). DiO&Dil@Plevs and the physical mixture of DiO@PMV/Dil@Levs were incubated with HUVEC cells for 6 h, respectively. The cells were then stained with DAPI and imaged using confocal microscopy.

2.5. In vitro release

To evaluate the *in vitro* release of Fer-1, 1.0 mL of free Fer-1, Fer-1@PLevs, and Fer-1@PLevs-C&U were placed in a dialysis bag with an MWCO of 25 kDa, respectively, and incubated with 20 mL of the 0.1% SDS-containing PBS buffer solution (pH 7.4) as release medium. The release study was investigated in the shaker at 37 °C at 100 rpm. At different time intervals, 1 mL of release buffer was withdrawn, and an equal amount of fresh release medium was replenished. The concentration of released Fer-1 was analyzed using the HPLC assay under the same conditions described above.

To evaluate the *in vitro* release of UPA, 1.0 mL of free UPA, Fer-1@PLevs-U, and Fer-1@PLevs-C&U were placed in a dialysis bag with an MWCO of 30 kDa, respectively, and incubated with 20 mL of the 0.1% (*w/v*) SDS-containing PBS buffer solution (pH 7.4) as release medium. The release study was investigated in the shaker at 37 °C at 100 rpm. At different time intervals, 1 mL of release buffer was withdrawn, and an equal amount of fresh release medium was replenished. The concentration of released UPA was analyzed using the UPA ELISA assay kit under the same conditions described above.

2.6. Platelet aggregation study

To investigate the aggregation activity of the Fer-1@PLevs-C&U, 1 mL of platelet-rich plasma (PRP) was prepared from human whole blood with sodium citrate as the anti-coagulant and placed into the 24-well plate. One mL of saline, PMV, and Fer-1@PLevs-C&U were subsequently added to the PRP solution. The 24-well plates were immediately placed in an EnVision Multilabel Reader and monitored for a change in absorbance at 650 nm over time. The thrombin was added to PRP to induce platelet aggregation as a positive control. The platelet aggregation was observed based on the reduction of turbidity.

2.7. Hemolysis test

Whole blood was collected in an ethylene diamine tetraacetic acid (EDTA) anti-coagulant tube. The red blood cells were obtained by centrifuging at 120×*g* for 10 min. The Fer-1@PLevs-C&U with different concentrations (0.2, 0.4, 0.6, 0.8, and 1.0 mg/mL) were incubated with a suspension of red blood cells at 37 °C for 2 h and then centrifuged at 1500 rpm for 10 min. The suspension of red blood cells incubated with ultrapure water and saline was set as the positive and negative control groups, respectively. The absorbance of the supernatant was measured at 570 nm with a microplate reader.

2.8. In vitro cytotoxicity

HUVEC cells were seeded in a 96-well plate at a density of 4×10^3 cells per well. The HUVEC cells were counted using a Countstar automated cell counter (Countstar Mira FL, Shanghai, China). After overnight incubation, a cell culture medium containing various drug-loaded formulations (PBS, Fer-1@PMV, Fer-1@PLevs, Fer-1@PLevs-C, Fer-1@PLevs-C&U) with different Fer-1 concentrations (1, 2, 4, 6, 8, 10 μmol/L) was added to the cells for 24 and 48 h incubation at 37 °C, respectively. At the end of the incubation period, the cell viability was evaluated using the MTT assay, following the manufacturer's instructions.

2.9. Cellular uptake

2.9.1. Cell uptake mechanism

The competitive inhibition assay is a method that involves the addition of specific competing molecules to block target endocytic pathways or the binding of specific receptors, thereby evaluating the role of different endocytic pathways in nanoparticle uptake processes and providing preliminary evidence for mechanistic studies.

The cellular uptake mechanism of Fer-1@PLevs-C&U was investigated in damaged HUVEC cells. Logarithmic growth phase HUVEC cells were seeded in 6-well plates (2 mL/well), and after they grew to 80%, 1 μg/mL LPS was added to 10% DMEM for co-incubation for 2 h. After incubation with endocytosis inhibitors (chlorpromazine, methyl-β-cyclodextrin, amiloride, 4 °C) in the complete medium for 2 h, fluorescently labeled Fer-1@PLevs-C&U was added and incubated for another 2 h ($n = 6$). Unuptaken formulations were washed away with pre-cooled PBS, and the cells were digested with trypsin and centrifuged to prepare single-cell suspensions for flow cytometry analysis.

The cellular uptake mechanism of Fer-1@PLevs-C&U was investigated in inflammatory RAW264.7 cells. Logarithmic growth phase RAW264.7 cells were seeded in 6-well plates (2 mL/well), and after they grew to 80%, 0.1 μg/mL LPS was added to 10% DMEM for co-incubation for 12 h. After incubation with endocytosis inhibitors (chlorpromazine, methyl-β-cyclodextrin, amiloride, 4 °C) in the complete medium for 2 h, fluorescently labeled Fer-1@PLevs-C&U was added and incubated for another 2 h ($n = 6$). Unuptaken formulations were washed away with pre-cooled PBS, and the cells were digested with trypsin and centrifuged to prepare single-cell suspensions for flow cytometry analysis.

2.9.2. Cellular uptake of HUVEC

The cellular uptake of platelet membrane-derived carriers (DiO, DiO@Lipo, DiO@Levs, DiO@PMV, DiO@PLevs, DiO@PLevs-C) was investigated in HUVEC cells. HUVEC cells were seeded in 6-well plates at a density of 3×10^5 cells per well and incubated with serum-free DMEM diluted platelet membrane-derived carrier for 1, 3, and 6 h, respectively. After incubation, the cells were washed with PBS, and the intracellular fluorescence signal was analyzed using the flow cytometer (BD FACSVerse, USA).

To further observe the intracellular localization of platelet membrane carriers (DiO, DiO@Lipo, DiO@Levs, DiO@PMV, DiO@PLevs, DiO@PLevs-C), HUVEC cells were seeded at a density of 2.5×10^5 cells in confocal culture dishes for 24 h and then incubated with the dye-containing carriers for 6 h. After that, cells were washed with PBS, fixed with paraformaldehyde, stained with DAPI, and imaged using confocal microscopy.

2.9.3. Cellular uptake of RAW264.7

The cellular uptake of platelet membrane-derived carriers was further investigated in active macrophages. RAW264.7 cells were incubated with 100 ng/mL LPS for 24 h and then seeded in 12-well plates at a density of 2×10^5 cells per well. Cells were co-incubated with FITC@PMV and FITC@PLevs (with PMV:Levs ratios of 10:1 and 20:1) for 6 or 12 h, respectively. After incubation, the cells were washed with PBS, and the intracellular fluorescence signal was analyzed using the flow cytometer.

To further observe the intracellular localization of platelet membrane carriers, RAW264.7 cells were seeded at a density of 2.5×10^5 cells in confocal culture dishes for 24 h and then incubated with the dye-containing carriers (FITC, FITC@PMV, FITC@PLevs, and Fer-1@PLevs-C) for 12 h. After that, cells were washed with PBS, fixed with paraformaldehyde, stained with DAPI, and imaged using confocal microscopy.

2.10. In vitro anti-inflammatory

2.10.1. ROS scavenging capacity

HUVECs were seeded in a 12-well plate at 2×10^5 cells per well and stimulated with 1 μg/mL LPS for 24 h. Platelet membrane carriers (Fer-1, Levs, Fer-1@PMV, Fer-1@PLevs, and Fer-1@PLevs-C&U) were added to wells and cultured with cells for 12 h. The activated HUVECs with DMEM medium were set as the model group, and the untreated HUVECs as the control group. After incubation, cells were washed with PBS and incubated with 0.5 mL DCFH-DA solution (50101ES01, Yeasen) for 30 min at 37 °C in the dark. The ROS levels were quantified using the flow cytometer.

2.10.2. Macrophage polarization

RAW264.7 cells were seeded in 6-well plates at 2.5×10^5 cells/well and incubated for 24 h. Cells were incubated with 100 ng/mL LPS for 24 h and then incubated with Fer-1@PMV, Fer-1@PLevs, Fer-1@PLevs-C, Fer-1@PLevs-C&U (Equivalent to 5 μmol/L of Fer-1) for 6 h. After incubation, cells were collected, washed, and stained with CD86-PE and CD206-APC antibodies. The cells were analyzed using the flow cytometer.

2.11. In vitro targeting ability

The *in vitro* targeting ability of Fer-1@PLevs-C&U was evaluated by constructing thromboses *in vitro*. To prepare the thrombus blocks, whole arterial blood was mixed with calcium chloride solution (20 mmol/L) and thrombin solution (10 μmol/L) and placed in a black 96-well plate. The mixture was then incubated at 37 °C for 3 h to form a preliminary thrombus block and then stored at 4 °C for 2 days to create a stable thrombus block. PBS, free DiD, DiD@Lipo, DiD@Levs, DiD@PMV, DiD@PLevs, and DiD@PLevs-C solutions (equivalent DiD concentration, 10 μmol/L) were added to the wells containing thrombus and incubated at 37 °C for 2 h. Then, the thrombus blocks were washed and observed using the Tanno *in vivo* optical imaging system (excitation wavelength of 646 nm, emission wavelength of 663 nm). The fluorescence intensity within the thrombus was quantitatively analyzed using quantitative analysis.

2.12. In vitro thrombolytic ability

The prepared thrombuses were weighed, placed in 12-well plates, and randomly divided into five groups. The platelet membrane-wrapped carriers (PBS, UPA, Fer-1@PLevs-C, Fer-1@PLevs-U, Fer-1@PLevs-C&U) with equal UPA concentration (40 μg/mL) were added into the wells. The weights and appearances of the clots were observed at 37 °C for 0, 1, 2, 3, and 4 h after incubation. The thrombolytic efficiency of each group was calculated according to Eq. (1).

$$\text{Thrombolysis rate}\,(\%) = \frac{W - W_i}{W} \times 100\% \quad (1)$$

where W represents the mass of the thrombus before thrombolysis, and W_i represents the weight of the thrombus in each group at different time points.

2.13. In vivo thrombus targeting ability

All animal experiments were approved by the Institutional Animal Care and Use Committee (IACUC) of the Animal Experiment Center of China Pharmaceutical University (No. 20190515-007). The mouse arterial thrombosis model was established by inducing endothelial damage by co-incubating 10% $FeCl_3$ with the mouse carotid artery vessels. The normal carotid artery on the opposite side of the mice was used as the control group. Fluorescent dye-containing platelet membrane warped carriers (DiD, DiD@Lipo, DiD@PMV, DiD@Levs, DiD@PLevs-C, DiD@PLevs, DiD@PLevs-C, and DiD@PLevs-C) (equal DiD content of 90 μg/mL) were administered to the mice *via* intravenous injection. The mice were then placed in the Tanno Small Animal *in vivo* Imaging System to capture images of the carotid arteries on both sides, and the fluorescence intensity was recorded at 0, 10, 20, 30, 45, and 60 min after injection. The mice were then euthanized, and both arteries and major organs were collected and analyzed for fluorescence intensity using quantitative software.

2.14. In vivo thrombolysis ability

Healthy ICR mice were randomly divided into eight groups ($n = 3$): (1) PBS, (2) UPA, (3) PMV-U, (4) PLevs-U, (5) PLevs-C&U, (6) Fer-1@PLevs-C&U, (7) Fer-1@PLevs-C, (8) Fer-1@CLipo&U. When the carotid artery thrombosis model was established, mice were injected with different formulations *via* intravenous injection. Then, the mice were placed under a laser speckle blood flow imaging system (Moor FLPI-2) for continuous monitoring after 0, 5, 10, 15, and 20 min after injection, respectively. The blood flow status was quantitatively determined using quantitative analysis software. The state of thrombus dissolution and generation in the blood vessel was determined.

2.15. In vivo thrombus recurrence

The study involved a total of 30 mice that were randomly divided into 6 groups ($n = 3$): UPA, PMV-U, PLevs-U, PLevs-C&U, Fer-1@PLevs-C&U, and Fer-1@CLipo&U (equal UPA of 180 μg/30 g). When the carotid artery thrombosis model was established,

mice were injected with different formulations *via* intravenous injection. Then, the mice were monitored by the laser speckle blood flow imaging system (Moor FLPI-2) until the blood flow was recovered in the artery. After 24 h after the injection, the mice were anaesthetized, and the damaged carotid arteries were exposed again to observe the blood flow. After that, the mice were euthanized, and the damaged carotid arteries were collected and stained by H&E to assess the obstruction rate.

The expression of key inflammatory factors, endothelial cell surface proteins, and anti-inflammatory factors was also examined. The carotid arteries were washed with PBS, fixed with paraformaldehyde, and embedded in paraffin wax. The expression of interleukin-6 (IL-6), tumor necrosis factor (TNF-α), endothelial nitric oxide synthase (eNOS), and interleukin-10 (IL-10) was examined by immunofluorescence staining.

2.16. *Pharmacokinetics test of Fer-1@PLevs-C&U*

uPA, Fer-1, and Fer-1@PLevs-C&U were injected into the tail vein of rats (UPA dose: 1 mg/kg; Fer-1 dose: 0.8 mg/kg) ($n = 3$). Blood samples were collected from the retroorbital plexus at 1, 10, 20, 30 min, 1, 2, 4, 8, 12, and 24 h after injection. To minimize the hydrolysis of Fer-1, the whole blood was placed on ice for 30 min and then centrifuged. The collected serum was stored at -80 °C for further analysis. The content of UPA was determined using an ELISA kit according to the manufacturer's instructions. For Fer-1 analysis, serum and acetonitrile were mixed at a ratio of 1:1 to precipitate proteins. After filtration, the liquid phase was analyzed by HPLC with acetonitrile: water (50:50) as the mobile phase at a flow rate of 1 mL/min and a detection wavelength of 254 nm.

2.17. *Safety evaluation*

Mice were randomly divided into 8 groups ($n = 3$): (1) PBS, (2) UPA, (3) PMV-U, (4) PLevs-U, (5) PLevs-C&U, (6) Fer-1@PLevs-C&U, (7) Fer-1@PLevs-C, (8) Fer-1@CLipo&U. The mice in each group were administrated the different formulations *via* intravenous injection and their body weight were monitored until seven days later. Then, the mice were euthanasia, and the blood was collected. The plasma was isolated, and the content of fibrinogen concentration (Fg) was analyzed using an automatic coagulation analyzer (PERLONG PUN-2048A). The major organs of mice were collected and stained with H&E. The images of H&E slices were collected to determine the safety of formulations.

2.18. *Statistical analysis*

The statistical analysis was executed using the conventional Student's *t*-test to compare two individual groups and One-Way ANOVA to analyze more than two groups, with a minimum confidence level of 0.05 for identifying statistically significant differences. The results were expressed in terms of the mean and standard deviation.

2.19. *Target prediction and functional analysis*

Potential targets of action of Ferrostatin-1 were predicted by the SwissTargetPrediction platform, and all predicted targets were normalized using the UniProt database. Potential targets for thrombosis-related cardiovascular diseases were retrieved from the GeneCards database. The potential therapeutic target genes of Ferrostatin-1 in the most representative myocardial infarction and ischemic stroke were screened by taking the intersection of compound targets and disease targets. Subsequently, the cross-targets were imported into the STRING database to construct a protein-protein interaction (PPI) network, and visualized and analyzed using Cytoscape software (version 3.10.2, Institute for Systems Biology, USA). The cross-targets were analyzed for functional enrichment using the Metascape database. Finally, the relevance of core target genes to multiple cardiovascular diseases was assessed with the help of the CVD Atlas database.

3. Results and discussion

3.1. *Characterization of Fer-1@PLevs-C&U*

Platelets are a type of non-nucleated cell produced by the bone marrow megakaryocytes. In their natural state, they are typically disc-shaped, with a slightly convex appearance. As shown in Fig. 1A and B, when platelet solution is placed on a slide and viewed under an orthostatic fluorescence microscope, it displays a stacked arrangement of spherical cells that range in size from 2 to 5 μm. Platelets stained with Wright's dye solution reveal grey-blue globular cells, as illustrated in Fig. 1C. SDS-PAGE experiments demonstrate that the protein bands on the surface of platelet membranes (IV and V) obtained through the repeated freeze-thaw method are consistent with those of freshly extracted platelets (Fig. 1D). Furthermore, the particle size of probiotic vesicles (Levs) is approximately 114.1 ± 3.8 nm, displaying a spherical membrane vesicle structure, and the surface of Levs contains specific proteins associated with probiotics. The drug loading of Fer-1 in Fer-1@Plevs was determined by HPLC to reach 2.12 ± 0.17% with an encapsulation rate of 55.17 ± 4.32% (Supporting Information Tables S1 and S2).

Fer-1@PLevs-C&U was synthesized by conjugating UPA outside of the Fer-1@Plevs. The successful binding of UPA to the platelet membranes was verified by measuring changes in the amounts of surface thiol groups and UPA concentration. Results showed that the surface thiol content of Fer-1@PLevs-C&U was only 55.8% of that of Fer-1@PLevs, indicating the successful conjugation of UPA (Supporting Information Fig. S1). When the ratio of UPA incorporation to platelet membrane proteins in Fer-1@PLevs was 1:1, the concentration of UPA on the surface of Fer-1@PLevs-C&U reached a maximum of 269.63 ± 17.60 μg/mL (Supporting Information Fig. S2 and Table S3).

As the complexity of carrier preparation escalates (PMV, PLevs, Fer-1@PLevs, Fer-1@PLevs-C&U), both the particle size and ζ-potential exhibit systematic variations (Supporting Information Table S4, and Fig. S3). The particle size of Fer-1@PLevs-C&U was 180.6 ± 7.2 nm (Fig. 1E, Fig. S3D), with a PDI of 0.392 ± 0.020. The TEM images suggested that the morphology of Fer-1@PLevs-C&U exhibited a spherical bilayered vesicle structure. As shown in Fig. 1F, platelet-based vesicles displayed similar UV absorption patterns, including Fer-1@PLevs-C&U. While the insertion of CREKA and coupling of UPA-SMCC caused a slight blue shift of the UV absorption peaks of hybridized vesicles at 220 nm. Physical stability evaluation exhibited that the particle size of Fer-1@PLevs-C&U remained within the range of 250 to 320 nm, and the potential remained around -18 mV without apparent fluctuations after being stored at 4 °C for one week, indicating good stability under the above storage conditions (Fig. 1G). Western blotting assay showed that the membrane proteins on the surface of the platelet membrane-

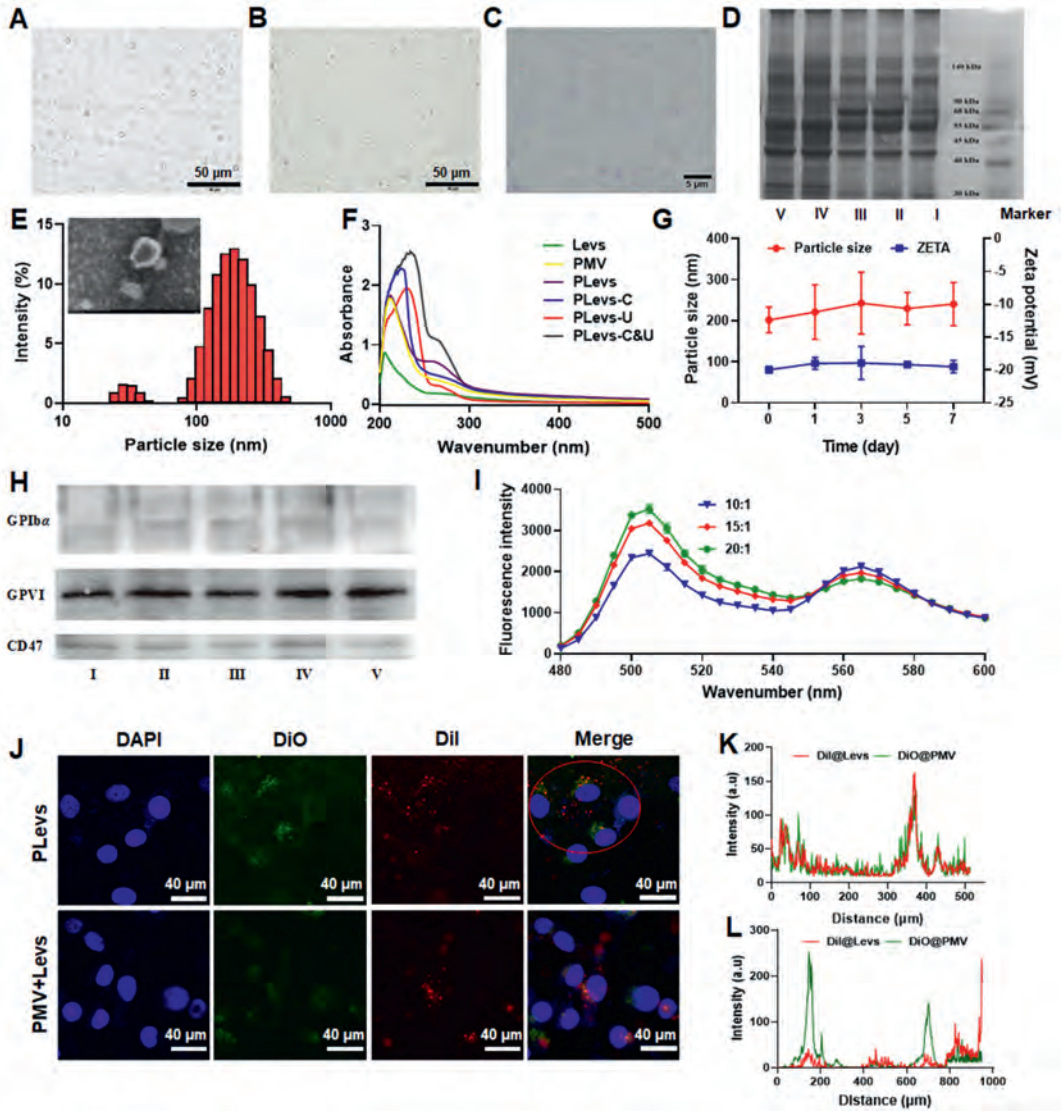

Figure 1 Synthesis and characterization of Fer-1@PLevs-C&U. Microscopy images of (A) PRP solution, (B) extracted platelets, and (C) the platelets stained with Wright's dye solution. (D) SDS-PAGE picture of extracted PMs (I−III: Platelet; IV: PM extracted from freeze-thaw in 4 °C; V: PM extracted from freeze−thaw in −20 °C). (E) Size distribution and TEM image of Fer-1@PLevs-C&U. (F) UV spectrum scan of Levs, PMV, PLevs, PLevs-U, and PLevs-C&U. (G) The variations in particle size and zeta potential of Fer-1@PLevs-C&U stored at 4 °C ($n = 3$). (H) The protein bands of GPIbα, GPVI, and CD47 in I: Platelet, II: PMV, III: PLevs, IV: Fer-1@PLevs-U, and V: Fer-1@PLevs-C&U. (I) The fluorescence intensity of PLevs in different ratios of $M_{DiO@PMV}$: $M_{DiI@Levs}$ ($n = 3$). (J) The CLSM picture of HUVEC incubated with DiI@Levs and DiO@PMV. (Scale bar = 40 μM) (K&L) The colocalization analysis of fluorescence in PLevs and physical mixture by ImageJ.

constructed nanocarriers were intact, with no difference in GPVI, GPIbα, and CD47 expression on the platelet membrane (Fig. 1H).

3.2. *Membrane fusion assay*

To verify the successful membrane fusion of Levs and PMV, we used the FRET assay to characterize differences in fluorescence signals. As shown in Fig. 1I, the excitation of DiO resulted in fluorescence emission of DiI. Moreover, with increasing amounts of DiO-labeled PMV in the hybrid vesicle, the fluorescence emission intensity of DiO was gradually restored, while the fluorescence emission intensity of DiI was slightly reduced, which indicates that the ratio of the fusion between the two membranes gradually approached saturation. The membrane fusion was further confirmed by confocal microscopy. The fluorescence signals of DiO and DiI largely overlapped, indicating that PMV and Levs have been successfully fused (Fig. 1J). We further used ImageJ to analyze the signals of DiO and DiI in Fig. 1J. The data confirmed significant overlap of DiO and DiI signals in the selected area in PLevs groups, but not in the physical mixture group (Fig. 1K−L).

3.3. *In vitro release of Fer-1@PLevs-C&U*

The Fer-1 release curves from different formulations in a pH 7.4 release medium are investigated. As shown in Fig. 2A, free Fer-1 exhibited swift and complete release, with cumulative release rates of 68.20 ± 6.15% and 89.50 ± 0.71% at 24 and 48 h,

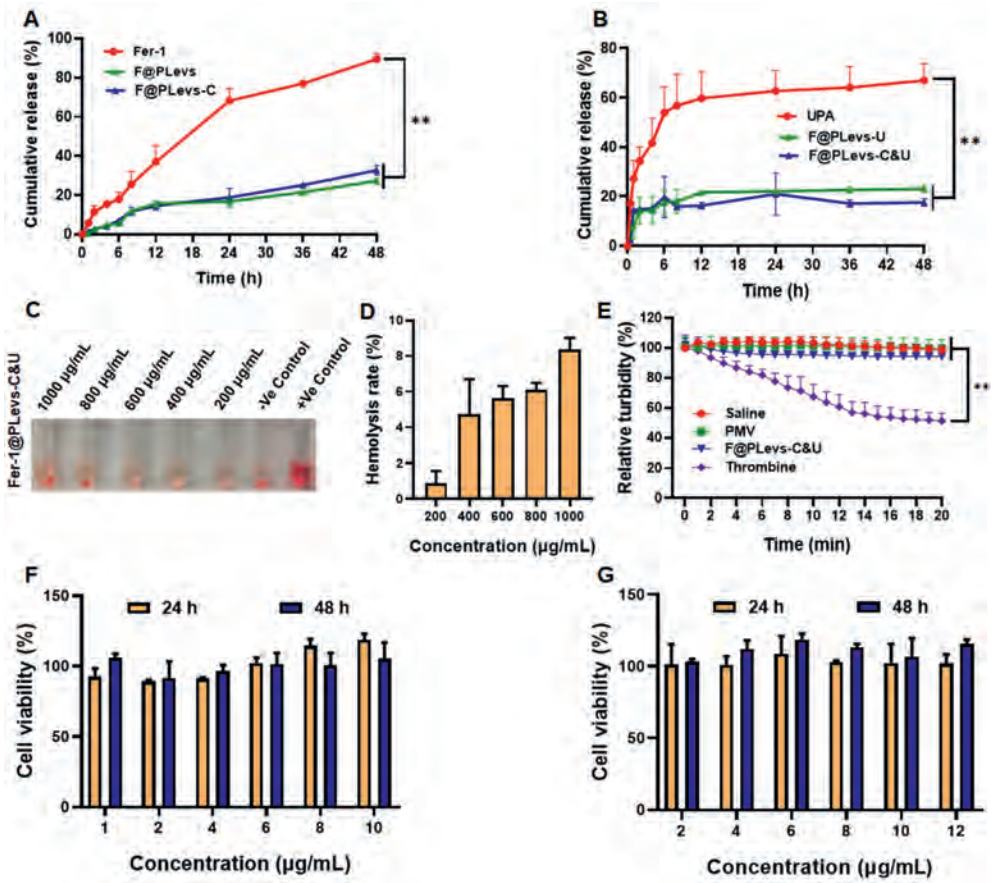

Figure 2 *In vitro* release and biocompatibility evaluation of Fer-1@PLevs-C&U. (A) Cumulative drug release profiles of Fer-1, Fer-1@PLevs, and Fer-1@PLevs-C in PSB (contains 0.1% SDS) at pH 7.4 ($n = 3$, $^{**}P < 0.01$). (B) Cumulative drug release profiles of UPA, Fer-1@PLevs-U, and Fer-1@PLevs-C&U in PSB (contains 0.1% SDS) at pH 7.4 ($n = 3$, $^{**}P < 0.01$). (C, D) The hemolysis images and calculated hemolysis rate ($n = 3$) of Fer-1@PLevs-C&U at different concentrations. (E) Platelet aggregation rate of different formulations ($n = 3$, $^{**}P < 0.01$). (F) The cell viability of Fer-1@PLevs-C&U against HUVEC for 24 and 48 h ($n = 3$). (G) The cell viability of Fer-1@PLevs-C&U against RAW264.7 cells for 24 and 48 h ($n = 3$).

respectively. The Fer-1@PLevs and Fer-1@PLevs-C groups both exhibited a slower release rate, with 2.50 ± 0.16% and 2.71 ± 0.27% release at 2 h, respectively, indicating that there was no burst release of the drug during the release process. Compared to the free Fer-1 group, the cumulative release of Fer-1 in the Fer-1@PLevs and Fer-1@PLevs-C groups was 16.75 ± 2.61% and 18.82 ± 4.64% at 24 h and 27.23 ± 1.42% and 32.67 ± 3.31% ($P < 0.05$) at 48 h, respectively, indicating the prolonged drug release behavior from the nano-formulations. The UPA release curves from different formulations in a pH 7.4 release medium are investigated. As shown in Fig. 2B, free UPA exhibited swift and complete release, with cumulative release rates of 64.06 ± 8.51% and 66.95 ± 6.77% at 24 and 48 h, respectively. The Fer-1@PLevs-U and Fer-1@PLevs-C&U groups both exhibited a slower release rate, with 21.19 ± 7.96% and 21.98 ± 0.26% release at 2 h, respectively, indicating that there was no burst release of the drug during the release process. Compared to the free UPA group, the cumulative release of UPA in the Fer-1@PLevs-U and Fer-1@PLevs-C&U groups was 33.92 ± 1.03% and 25.51 ± 0.26% at 24 h and 34.66 ± 1.03% and 26.05 ± 0.26% ($P < 0.05$) at 48 h, respectively, indicating the prolonged drug release behavior from the nano-formulations. The data indicated that the hybridized vesicles were stable at pH 7.4 without significant drug leakage, and also exhibited controlled release behavior. Moreover, the CREKA modification did not significantly affect the release characteristics of the vesicles.

3.4. *In vitro biocompatibility evaluation*

3.4.1. *Hemolysis test*

The *in vitro* biocompatibility of hybridized vesicles (Fer-1@PLevs-C&U) was investigated using the hemolysis assay. As shown in Fig. 2C and D, there was no significant lysis of the erythrocytes in the negative control group and incubated Fer-1@PLevs-C&U groups with various concentrations. The maximum concentration of hybrid vesicles in the study induced only a low hemolysis rate of less than 10%, suggesting that Fer-1@PLevs-C&U exhibits good biocompatibility.

3.4.2. *Platelet aggregation study*

To confirm that the hybrid vesicles would not lead to platelet aggregation, we co-incubated platelets with different formulations and observed the potential aggregate formation. As shown in Fig. 2E, platelets from the positive control group gradually delaminated and formed white flakes at the bottom, and their absorbance was reduced significantly. In contrast, the platelet

suspensions of the saline, PMV, and Fer-1@PLevs-C&U groups remained as milky-white suspensions without visible aggregation at the bottom, and the absorbance of the suspension at 650 nm showed no significant differences, which suggests good platelet compatibility of Fer-1@PLevs-C&U.

3.4.3. In vitro cytotoxicity

Here, we evaluated the cytotoxicity of formulations in both HUVEC and RAW 264.7 cells. As shown in Fig. 2F, the cell viability of HUVECs was higher than 90% when co-incubated for 24 or 48 h with Fer-1@PLevs-C&U at different Fer-1 concentrations. Moreover, no significant cytotoxicity was observed in RAW264.7 cells after incubation with Fer-1@PLevs-C&U (Fig. 2G). These all suggest that the Fer-1@PLevs-C&U has minimal impact on cell proliferation and apoptosis within the concentration range used in this study and demonstrates good biocompatibility.

3.5. Cellular uptake

3.5.1. Cell uptake mechanism

As depicted in Supporting Information Fig. S4, taking the fluorescence intensity of cells in the control group as a reference, the relative uptake rates of each treatment group were calculated. Under 4 °C conditions, both damaged HUVEC cells (Fig. S4A) and RAW cells (Fig. S4B) showed a significant reduction in relative uptake rates ($P < 0.01$). This indicates that lowering the temperature to inhibit cell metabolism and ATP production effectively blocked energy-dependent endocytosis. Moreover, after treatment with CPZ (chlorpromazine) and EIPA (amiloride), both HUVEC and RAW cells exhibited reduced uptake rate compared to the control group ($P < 0.01$). However, for cells treated with methyl-β-cyclodextrin, no significant difference in the relative uptake rate was observed compared to the control group. Consequently, these findings suggest that under the context of energy metabolism-dependent endocytosis, Fer-1@PLevs-C&U is primarily internalized *via* clathrin-mediated endocytosis and macropinocytosis.

3.5.2. Cellular uptake of HUVEC

As shown in Fig. 3A and B, the fluorescence intensity in HUVEC after incubation with different formulations increased over time in a time-dependent manner. Compared with the free DiO and DiO@Lipo groups, the cellular uptake of the DiO@PLevs was significantly enhanced at 6 h with higher fluorescence intensity, indicating that the uptake of heterogeneous carriers was improved in activated endothelial cells. Additionally, the insertion of the CREKA peptide further increased the uptake in the DiO@PLevs-C group at 6 h, with fluorescence intensity 1.21 times higher than DiO@PLevs. Similar results were observed using the confocal microscopy assay (Fig. 3C). Cells treated with DiO@PLevs-C exhibited the strongest green fluorescent signals among all groups after co-incubation, indicating that the nanocarriers were successfully internalized by the uptake of hybrid vesicles by endothelial cells. The conjugation of the CREKA peptide appears to enhance the uptake of hybrid vesicles by endothelial cells.

3.5.3. Cellular uptake of RAW264.7

The cellular uptake of macrophages was also investigated. Macrophages were first polarized into the M1 phenotype by LPS stimulation, and then incubated with FITC-labeled hybrid vesicles. To more precisely investigate the impact of the ratio of Levs to platelet membrane on cellular uptake, two groups were established, including PLevs-1 and PLevs-2, with mass ratios of Levs to platelet membrane protein of 1:20 and 1:10, respectively. As shown in Fig. 3D and E, the fluorescence intensity of the PLevs-2 group was 1.54 times higher than that in the PMV group after 12 h of incubation, which indicates that Levs enhanced the inflammation-targeting ability of the platelet vesicles. Additionally, laser confocal microscopy results (Fig. 3F) demonstrated that the fluorescence intensity in the FITC@PLevs-C group was higher than in the other groups. Both flow cytometry and confocal data confirmed the targeted uptake of Fer-1@PLevs-C&U by inflammation-activated macrophages.

3.6. In vitro anti-inflammatory effect

3.6.1. ROS scavenging capacity

The ROS levels in HUVECs were evaluated to determine their anti-inflammatory effects. As shown in Fig. 4A and B, HUVECs incubated with LPS exhibited the strongest fluorescence signals, suggesting the inflammatory cytokines induce intracellular ROS production, thus damaging endothelial cells. After treatment with free Fer-1, the fluorescence signals decreased by approximately 1.1-fold compared to the model group, confirming the anti-inflammatory effect of the ferroptosis inhibitor in HUVECs. Treatment with Levs alone also resulted in a 1.46-fold reduction in fluorescence signal, indicating its ROS-scavenging capability. Furthermore, incubation with Fer-1@PLevs-C&U significantly reduced ROS levels by approximately 2.8 times compared to the model groups, exhibiting the strongest anti-inflammatory ability. Moreover, the ROS generation in damaged cells was further evaluated using the DCFA-DH probe and observed by confocal microscopy (Fig. 4C). Consistent with the flow cytometry data, cells treated with Fer-1 and Levs showed reduced fluorescence signals compared to the control. The Fer-1@PLevs-C and Fer-1@PLevs-C&U groups exhibited similar abilities in inhibiting ROS generation, which showed the lowest ROS signals. The data indicated that the combination of Levs and Fer-1 may synergistically enhance anti-inflammatory effects in damaged endothelial cells, and that CREKA modification further supports ROS scavenging by improving cellular uptake of the hybrid vesicles.

3.6.2. Macrophage polarization

To explore the influence of Fer-1@PLevs-C on macrophage phenotype, we stained the M_1 and M_2 polarization markers of macrophages in LPS-induced RAW264.7 cells after incubation with various formulations. As shown in Fig. 4D and E, LPS-induced RAW 264.7 exhibited a CD86 positive rate of 73.0%, indicating their M1 polarization. After incubation with Fer-1 and Fer-1-loaded formulations, cells showed an increased expression of CD206, an M2 polarization marker, from 23.6% to over 85.0%. The data suggest that Fer-1 and Levs can promote the M_1 macrophage transformation to the anti-inflammatory M_2 phenotype through the combined anti-inflammatory effects of probiotic vesicles and Fer-1. Furthermore, CREKA modification enhances the anti-inflammatory efficacy of the vesicles by increasing macrophage uptake behavior, indicating that Fer-1@PLevs-C&U holds strong potential to improve the thrombotic microenvironment.

3.7. In vitro targeting ability

The DiD-labeled formulations were incubated with thrombus to determine their *in vitro* targeting ability. As shown in Fig. 4F and G, compared to the DiD@Lipo group, the fluorescence intensity in

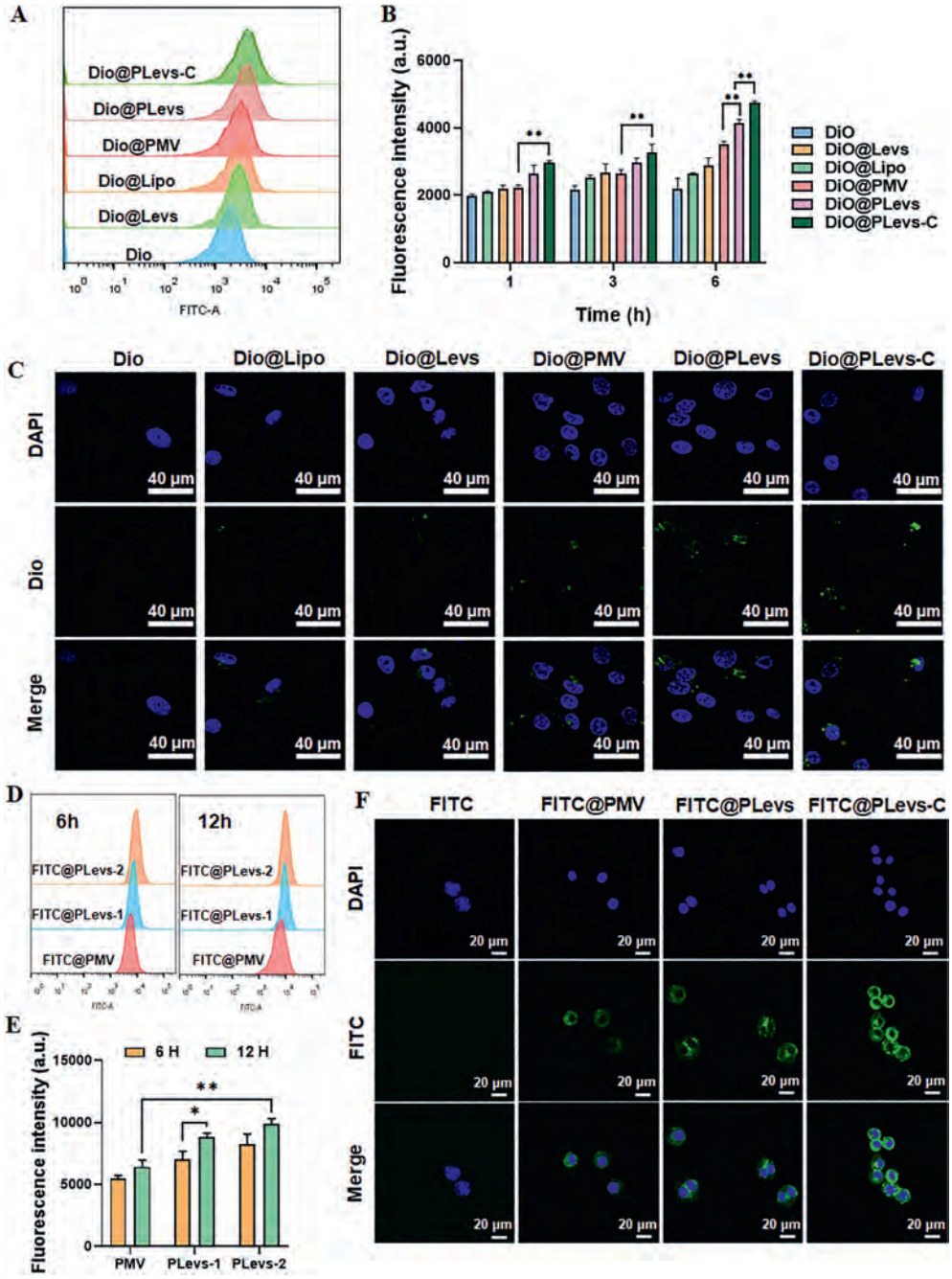

Figure 3 Cellular uptake of hybrid vesicles in HUVEC and M_1 subtype RAW264.7 cells. (A, B) Cellular uptake of DiO, DiO@Lipo, DiO@Levs, DiO@PMV, DiO@PLevs, and DiO@PLevs-C in HUVEC was measured by flow cytometry ($n = 3$, $^{**}P < 0.01$) and (C) by confocal assay. (D, E) Cellular uptake of FITC@PMV, FITC@PLevs-1, and FITC@PLevs-2 in RAW264.7 cells was measured by flow cytometry ($n = 3$) and by (F) by confocal assay.

DiD@Levs was significantly enhanced, which might be due to Levs binding to the multiple bacterial-binding receptors on the surface of the inflammatory cells inside the *in vitro* thrombus. The penetration of DiD@PMV into *in vitro* thrombus clots relies on GPIbα-mediated interactions with fibrinogen and inflammatory cells. Furthermore, the fluorescence intensity in thrombus clots from the DiD@PLevs-C groups was 1.61 times higher than that of the DiD@Levs group, suggesting that CREKA modification enhanced both the targeting efficiency and thrombus penetration of hybrid vesicles. This facilitated the delivery of the thrombolytic drug deep within the thrombus, ultimately resulting in more effective thrombolysis.

3.8. *In vitro thrombolysis assay*

The *in vitro* thrombolytic activity of Fer-1@PLevs-C&U was also investigated. After incubation with free UPA, Fer-1@PLevs-C, Fer-1@PLevs-C&U, and Fer-1@PLevs-U for 4 h, respectively, the volume of thrombus clots was significantly reduced to 78.95 ± 3.53 (Fig. 4H), which suggests that UPA, a thrombolytic

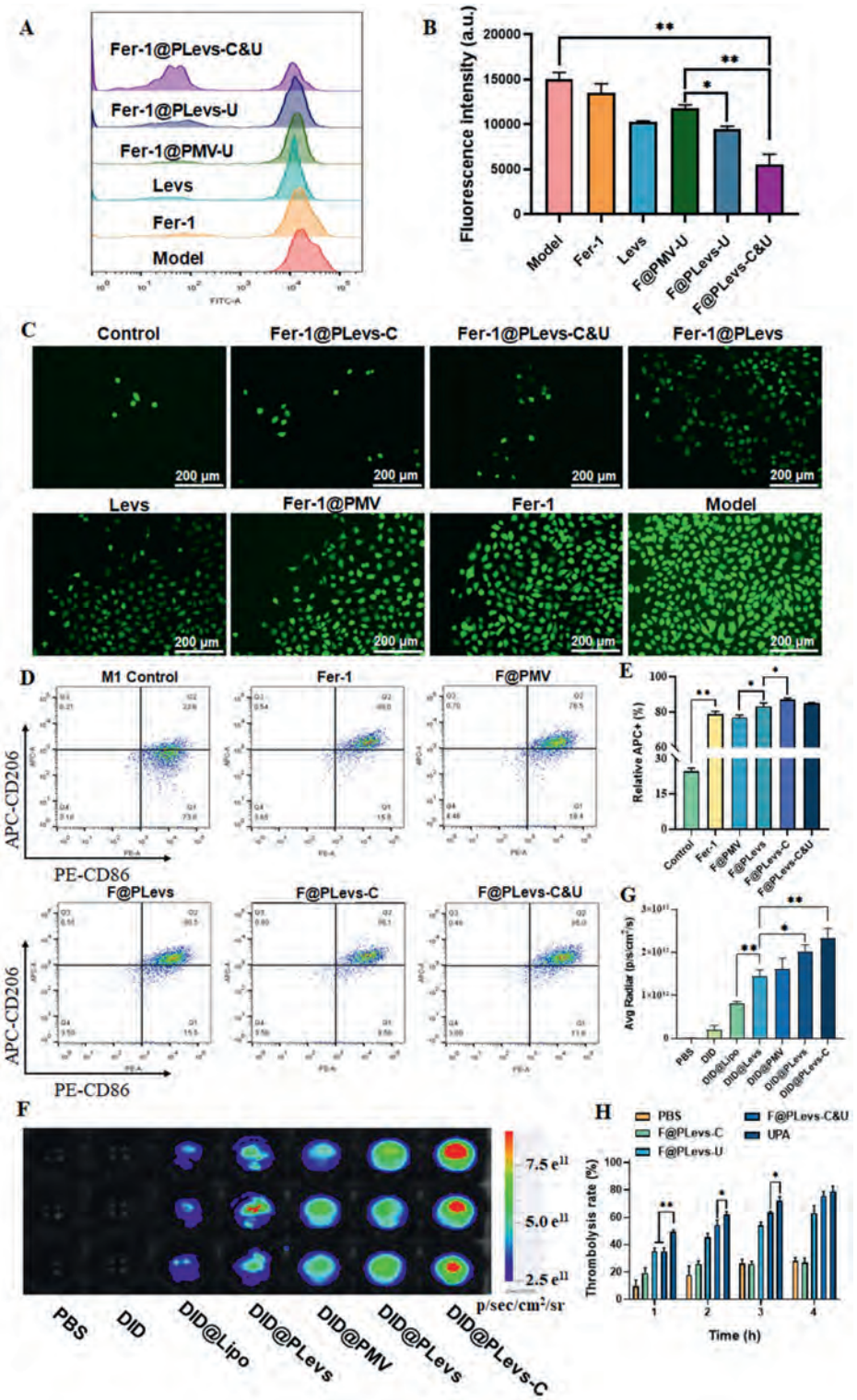

Figure 4 *In vitro* anti-inflammatory effect of Fer-1@PLevs-C&U. (A, B) Quantitative analysis of fluorescence intensity in damaged HUVEC after treatment with different formulations ($n = 3$, $^{*}P < 0.05$, $^{**}P < 0.01$). (C) The representative images of HUVECs after treatment with different formulations. The scale bars are 200 μm. (D, E) Representative FCM plots of re-educated macrophage and relative APC^{+} ratio ($n = 3$, $^{*}P < 0.05$, $^{**}P < 0.01$) after treatment with different formulations. (F, G) The representative images and semi-quantitative fluorescence intensity ($n = 3$, $^{*}P < 0.05$, $^{**}P < 0.01$) of blood clots after incubation with a different formulation. (H) The thrombolysis rate after incubation for various preparations ($n = 3$, $^{*}P < 0.05$, $^{**}P < 0.01$).

drug, can effectively and rapidly dissolve thrombus clots. Compared to the Fer-1@PLevs-U group, the Fer-1@PLevs-C&U group demonstrated superior thrombolytic performance, achieving a thrombolytic rate of 75.70 ± 3.11% after 4 h of incubation, which was compared to that of free UPA. We speculate that the fibrin-targeting peptide CREKA enhances the permeation and adhesion of hybrid vesicles within the thrombus to induce a higher rate of thrombolysis *in vitro*.

3.9. *In vivo thrombus targeting study*

The mouse arterial thrombosis model was established by inducing endothelial damage by co-incubating 10% $FeCl_3$ with mouse carotid artery vessels, and we used the thrombosis model mice for the *in vivo* targeting investigation. As shown in Fig. 5A, the fluorescence intensity in the carotid artery of the mice was constantly enhanced. In contrast, no noticeable fluorescence increase was observed in the undamaged carotid artery, indicating that the dye-loaded hybrid vesicles exhibited selective targeting of thrombi and damaged endothelial cells. For the DiD@PLevs-C group, the fluorescence intensity in the damaged carotid artery was 2.56 times and 4.01 times higher than that in the undamaged carotid artery after 20 and 60 min injection, respectively, which suggests that Fer-1@PLevs-C&U demonstrates strong thrombus-targeting capability in the damaged carotid artery *in vivo*. After the final observation point, the carotid arteries were isolated and washed for quantitative fluorescence analysis. As shown in Fig. 5B and C, the fluorescence intensity in the damaged vessels was higher than that of the undamaged carotid arteries in almost all the treatment groups. The fluorescence intensity in the damaged carotid arteries was 1.76 times higher than that of the damaged carotid arteries in DiD@PLevs-C groups, which was

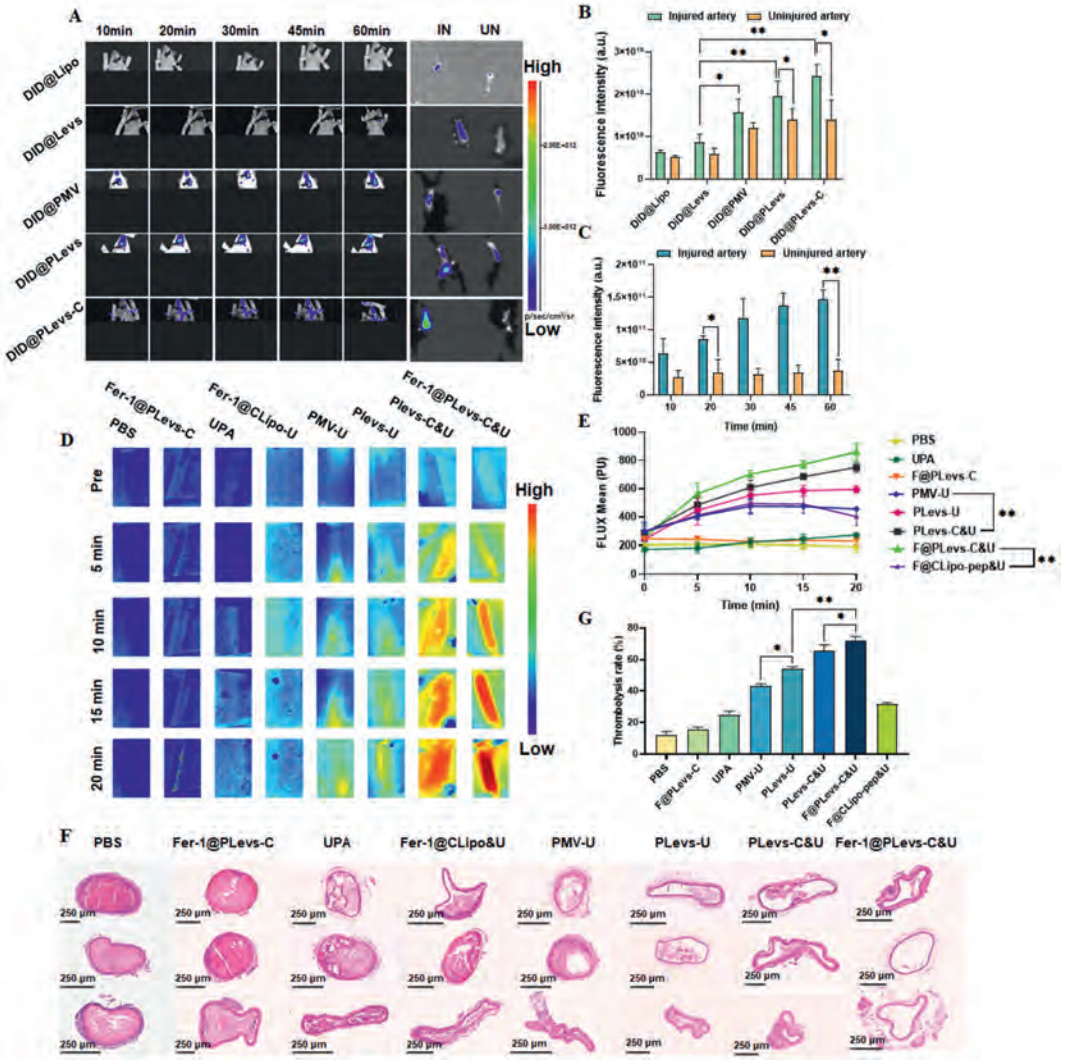

Figure 5 *In vivo* targeting and thrombosis ability of Fer-1@PLevs-C&U. (A) The representative IVIS images of mice (carotid artery parts) after administration with different formulations (IN and UN represent injured arteries and non-injured arteries). (B) Quantitative fluorescence intensity of bilateral carotid arteries of mice after administration with different formulations for 60 min ($n = 3$, $^{*}P < 0.05$, $^{**}P < 0.01$). (C) Fluorescence intensity of injured and uninjured carotid arteries in mice after administration with DiD@PLevs-C at various time points ($n = 3$, $^{*}P < 0.05$, $^{**}P < 0.01$). (D) Representative images of carotid blood flow were monitored before and 5, 10, 15, and 20 min after administration with different formulations. (E) Quantitative analysis of carotid blood flow after administration with different formulations ($n = 3$, $^{**}P < 0.01$). (F) H&E histopathological staining images and (G) percentage of thrombolysis rate of carotid arteries in mice after administration with different formulations ($n = 3$, $^{*}P < 0.05$, $^{**}P < 0.01$).

significantly higher than that in the DiD@PLevs group, suggesting that DiD@PLevs-C has improved thrombus selectively and penetration capability compared to other groups.

3.10. *In vivo thrombolysis ability*

A scatter flow imaging system was used to visualize carotid artery blood flow, and the blood flow was quantitatively analyzed using Moor FLPI-2 Review V6.0 software. As shown in Fig. 5D and E, the carotid blood flow images in the PBS group appeared blue during the investigation, indicating low blood flow and confirming that carotid thrombosis was successfully established. Meanwhile, the Fer-1@PLevs-C groups showed a similar low blood flow constitution, indicating that the Fer-1 alone had minimal effect on vessel recanalization. In the free UPA group, blood flow increased from 173.7 ± 3.85 PU (Perfusion Unit) to 273.2 ± 14.37 PU within 20 min, which suggests that UPA could reduce the thrombus burden, though the effect was short-lived. In contrast, blood flow in mice treated with PMV-U and PLevs-U gradually increased and stabilized by 15 min, reaching 455.7 ± 15.34 PU and 590.4 ± 19.33 PU, respectively.

In the Fer-1@PLevs-C&U group, blood flow increased rapidly and showed sustained time-dependent improvement following injection. It was observed that the blood flow gradually recovered to 860.1 ± 60.04 PU at 20 min after injection and remained at about 850 PU 1 h after injection. This outcome is likely due to the CREKA peptide, which enhances vesicle penetration into the thrombus and facilitates targeted release of the thrombolytic drug UPA, leading to their ablation.

Moreover, we stained the carotid thrombus with H&E to observe and quantify the vascular obstruction rate. As shown in Fig. 5F and G, compared with the free UPA group, the thrombolytic efficiency of PMV-U and PLevs-U was notably improved with thrombolytic rates of 43.04 ± 1.49% and 54.12 ± 1.32%, respectively. These results indicate that platelet membrane-based and probiotic hybrid carriers improve the thrombolytic efficiency of UPA at the thrombus site. The Fer-1@PLevs-C&U group exhibited the highest thrombolysis rates, reaching 71.68 ± 3.47%, which significantly reduced the vascular occlusion and enhanced recanalization of embolized vessels, consistent with the results of blood flow monitoring by scattered blood flow imaging.

3.11. *In vivo thrombus recurrence*

To evaluate the anti-recurrence efficiency, we administered UPA, Fer-1@CLipo&U, PMV-U, PLevs-U, PLevs-C&U, and Fer-1@PLevs-C&U at an equivalent but high UPA dose in the arterial thrombosis model mice at first to confirm that the original

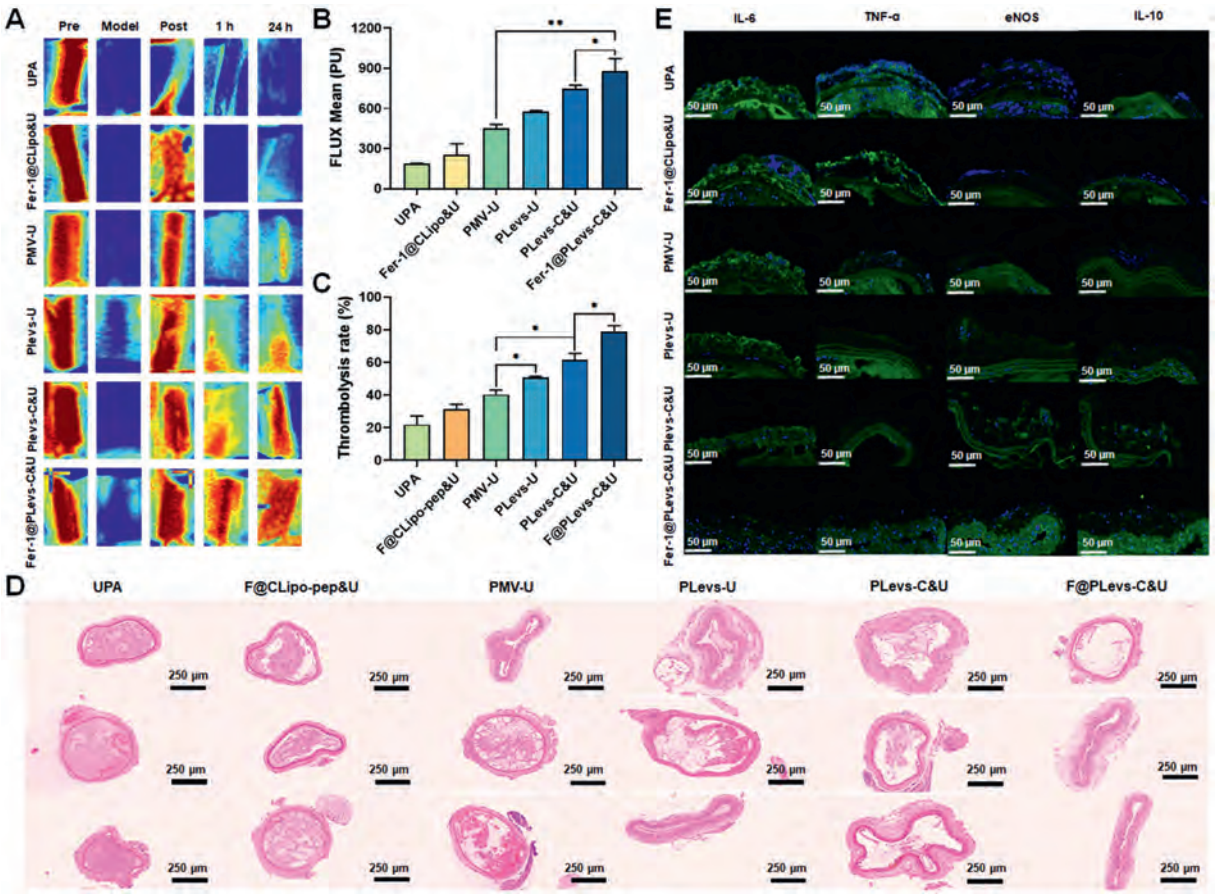

Figure 6 (A) Representative images and (B) quantitative analysis of carotid blood flow were monitored before modeling, after $FeCl_3$ incubation, and 15 min, 1, and 24 h after administration with different formulations ($n = 3$, $^*P < 0.05$, $^{**}P < 0.01$). (C) H&E histopathological staining results ($n = 3$, $^*P < 0.05$) and (D) percentage of thrombolysis rate of carotid arteries in mice after administration with different formulations. (E) Representative immunofluorescence images of eNOS, TNF-α, IL-10, and IL-6 expression in mice after administration with different formulations.

thrombus could be lysed. As shown in Fig. 6A and B, carotid artery blood flow was restored in all treatment groups following administration. Blood flow was then monitored over 24 h. In mice treated with free UPA or Fer-1@CLipo&U, blood flow began to decline within 1 h, and the vessels were nearly occluded by 24 h (186.3 ± 4.88 PU for the UPA group and 256.05 ± 81.92 PU for Fer-1@CLipo&U). In contrast, vascular blood flow in the PMV-U and PLevs-U groups reached 451.4 ± 29.94 PU and 574.0 ± 12.49 PU, respectively, at 24 h post-administration, indicating that the hybrid vesicles provided enhanced thrombus-site targeting and a longer-lasting therapeutic effect. When CREKA-modified hybrid vesicles were administered, blood flow levels at 24 h reached 747.95 ± 20.49 PU for the PLevs-C&U group and 880.5 ± 93.00 PU for the Fer-1@PLevs-C&U group, suggesting that CREKA modification improved both the penetration and retention of the formulation at the damaged endothelial site, supporting the controlled release of UPA and Fer-1.

A similar result was observed through H&E staining of the carotid arteries (Fig. 6C and D). In the UPA group and FER-1@CLipo&U group, thrombus clots nearly occluded the blood vessels, with blockage rates of 21.92 ± 5.24% and 31.59 ± 2.80%, respectively. These findings indicate that even though a high concentration of UPA can induce rapid thrombolysis driven by inflammatory factors, residual components at the thrombus site are prone to recur, posing a risk of secondary occlusion. In contrast, the PLevs-C&U and Fer-1@PLevs-C&U groups displayed a honeycomb-like structure in the carotid vessels, indicating that the fibrin network remained disrupted even 24 h after administration. The corresponding thrombolysis rates reached 61.50 ± 4.06% and 78.99 ± 3.56%, respectively, suggesting that Fer-1@PLevs-C&U provides a sustained thrombolytic effect on the thrombus network.

We further evaluated cytokine expression in the injured endothelial area. The levels of IL-6 and TNF-α in the carotid arteries of the Fer-1@PLevs-C&U group were significantly lower than those in the free UPA group (Fig. 6E), confirming the effective delivery of anti-inflammatory agents. This delivery helped regulate oxidative stress and substantially reduced both inflammatory cell recruitment and the secretion of proinflammatory cytokines triggered by endothelial dysfunction. Moreover, the carotid arteries in the Fer-1@PLevs-C&U group showed increased expression of eNOS and IL-10, suggesting that Fer-1@PLevs-C&U not only directly inhibits inflammation directly but also promotes the secretion of anti-inflammatory factors.

3.12. *Pharmacokinetics test of Fer-1@PLevs-C&U*

As shown in Supporting Information Fig. S5, we investigated the stability of Fer-1@PLevs-C&U under physiological conditions. In Fig. S5A, the concentration of free Fer-1 declined rapidly within 30 min and was barely detectable thereafter, whereas Fer-1 encapsulated in Fer-1@PLevs-C&U remained detectable for up to 24 h, indicating that Fer-1@PLevs-C&U prolongs the systemic retention time of Fer-1. Similarly, in Fig. S5B, the concentration of free UPA decreased sharply within 4 h, while UPA encapsulated in Fer-1@PLevs-C&U maintained a high level for at least 24 h. Therefore, it may prolong the retention time of iron UPA in the blood and exert its therapeutic effect for a more prolonged duration.

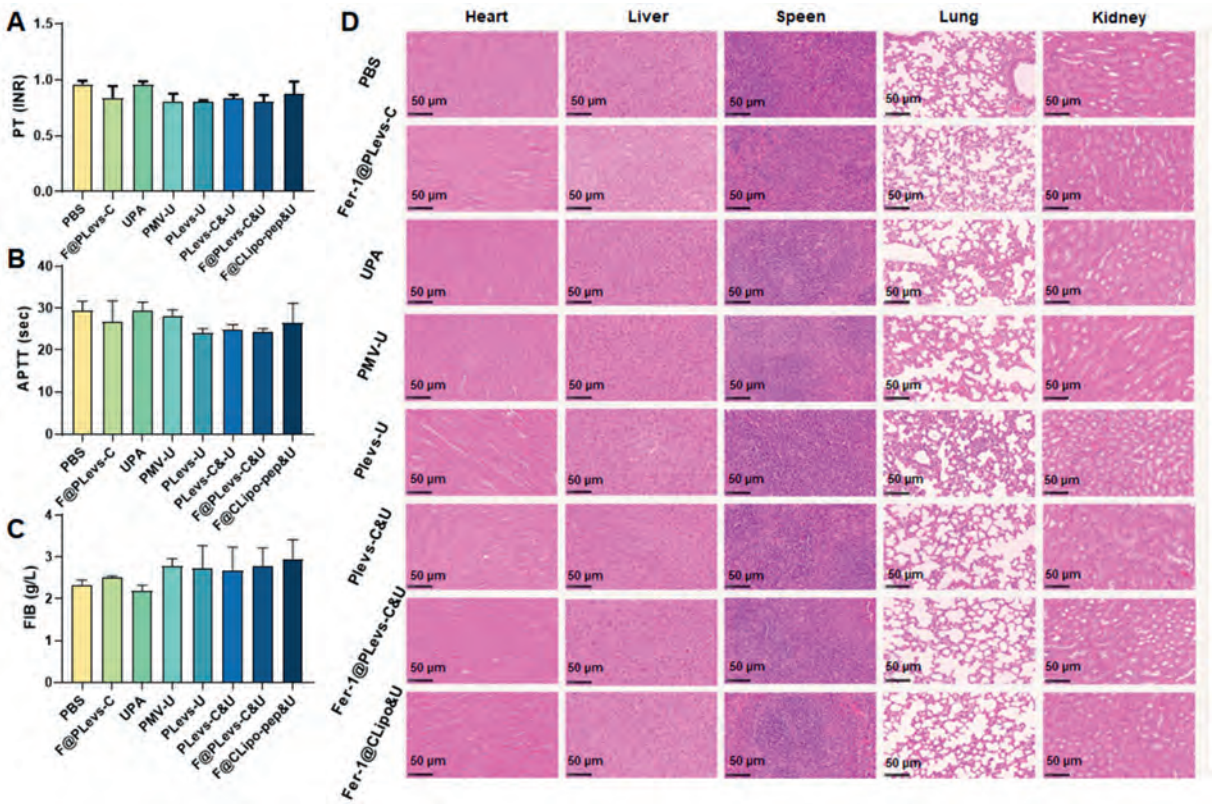

Figure 7 Safety evaluation of different formulations. (A−C) Blood parameters differ after injection of various formulations (n = 3, mean ± SD). (D) Analysis of H&E staining of heart, liver, spleen, lung, and kidney tissue sections at the end of continuous treatment of different formulations.

3.13. *Safety evaluation*

Different formulations were administered to mice to assess the safety of Fer-1@PLevs-C&U, and the changes in coagulation-related parameters were closely monitored. As shown in Fig. 7A–C, there were no significant fluctuations in the PT, APTT, and FIB levels of the mice from different formulation groups compared to the control group, indicating that Fer-1@PLevs-C&U is a biocompatible and safe nano preparation *in vivo*. Moreover, the histopathological examination shown in Fig. 7D revealed no apparent pathological changes, such as necrosis and inflammation, in the major organs of the mice administered with any of the preparations, further corroborating the good *in vivo* biocompatibility and safety of the prepared nano-preparations.

3.14. *Network pharmacology analysis*

To further explore the mechanisms by which Fer-1 regulates cardiovascular diseases caused by atherothrombosis, network pharmacology was employed as an integrative research approach to elucidate its multilevel regulatory mechanisms by analyzing its targets of action and their associated pathways. Based on the current study, one of the central roles of Fer-1 as an ferroptosis inhibitor lies in the regulation of the inflammatory microenvironment, particularly through modulating macrophage-associated inflammation. Through database searches, we obtained the possible targets of Fer-1 action and combined them with cardiovascular disease-related genes (key genes for atherosclerosis and thrombosis) for intersection analysis, and used these data to construct a target-disease pathway network, focusing on pathways related to ferroptosis, inflammation, and oxidative stress. Target intersection analysis revealed that Fer-1, myocardial infarction, and ischemic stroke shared 64 common targets (Fig. 8A). Gene set enrichment analysis of these 64 targets, performed using the Metascape bioinformatics platform (Fig. 8B), indicated significant involvement in the regulation of inflammation and immune response (GO:0050727, GO:0006954), cell migration and immune cell recruitment (GO:0050900), and oxidative stress following tissue injury (GO:0071248). These findings suggest that ferrostatin-1's inhibition of ferroptosis may enhance macrophage function by modulating these critical biological pathways.

We then analyzed the protein interactions of the 64 targets shared by Fer-1 with myocardial infarction and ischemic stroke using the STRING database (Search Tool for the Retrieval of Interacting Genes/Proteins) (Fig. 8C). Additionally, we used Cytoscape software to further visualize and analyze the interaction network of these targets (Fig. 8D). The interaction data obtained from STRING were screened to identify core targets, revealing that EGFR plays a critical role in vascular endothelial repair and inflammation regulation, suggesting that ferrostatin-1 may enhance endothelial cell function and reduce tissue ischemic injury *via* EGFR-related pathways. Similarly, CXCR4 was identified as a key regulator of macrophage recruitment and polarization, which may influence the inflammatory response and tissue repair processes following injury. These findings indicate that ferrostatin-1 may indirectly modulate macrophage function by affecting CXCR4 activity, further supporting the proposed mechanism by which Fer-1@PLevs-C&U inhibits thrombus recurrence, validating the therapeutic strategy developed in this study.

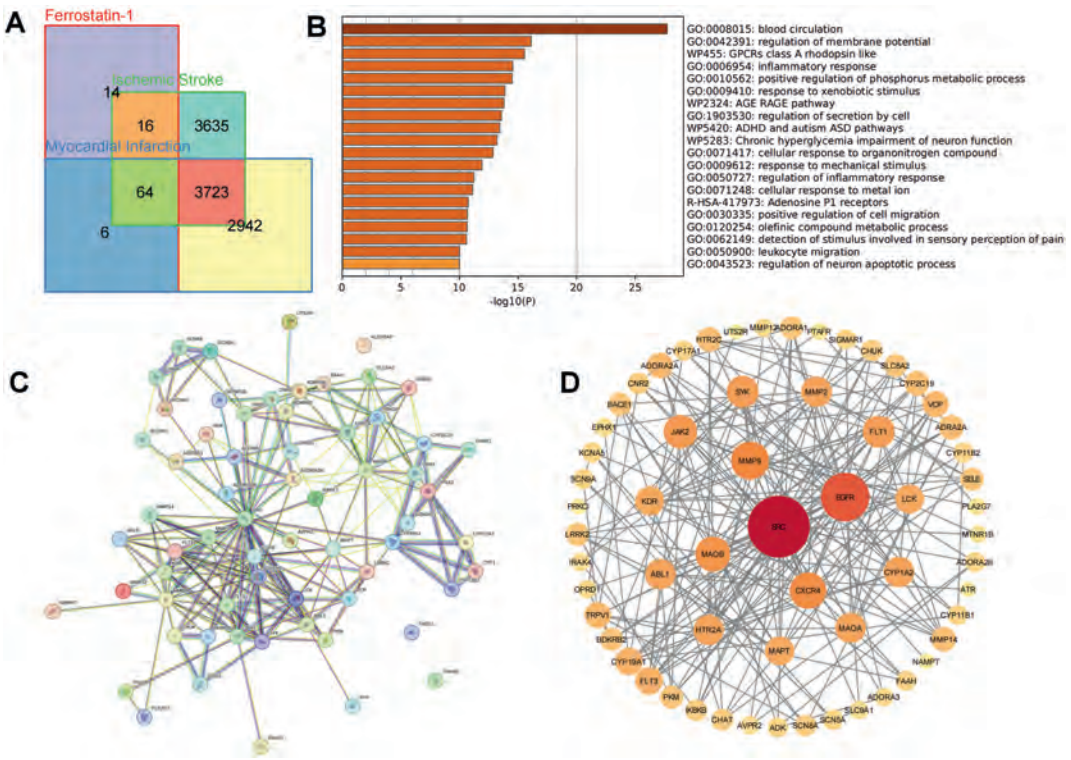

Figure 8 (A) Intersection analysis of Fer-1 and arterial vascular disease-related targets. (B) Intersection analysis of target gene enrichment. (C) Intersection analysis of target protein interaction. (D) Core target screening visualization analysis.

4. Conclusions

In summary, we designed CREKA peptide-modified hybrid vesicles (PLevs-C) by extrusion of platelet membranes and *Lactobacillus plantarum*-derived probiotic vesicles (Levs) and employed them for the co-delivery of Fer-1 and UPA. The resulting drug-loaded hybrid vesicles (Fer-1@PLevs-C&U) demonstrated the potential for effective and targeted delivery of thrombolytic agents to thrombus sites. UPA could be rapidly released to restore vessel patency, thus achieving efficient and precise thrombolysis, while Fer-1 contributed to modulating the inflammatory microenvironment and inhibited thrombus recurrence.

Acknowledgments

This study was supported by the National Natural Science Foundation of China (Grant No. 81972892) and Regional University−Industry Technology Transfer Center for Biopharmaceuticals (Nanjing, Jiangsu) Early-Stage Translational Grant (Grant No. JB2025211, China).

Author contributions

Yan Shen, Tianjiao Hao, Bin Gao and Chang Liu designed the research. Tianjiao Hao, Chuanjiang Ran, Bin Gao, Binghua Chang and Yuanyuan Zhou carried out the experiments and performed data analysis. Wei You participated part of the experiments. Jun Ye provided experimental drugs and quality control. Tianjiao Hao and Chang Liu wrote the manuscript. Yan Shen, Jun Ye and Qiyue Wang revised the manuscript. All of the authors have read and approved the final manuscript.

Conflicts of interest

The authors have no conflicts of interest to declare.

Appendix A. Supporting information

Supporting information to this article can be found online at https://doi.org/10.1016/j.apsb.2026.01.014.

References

1. Mensah GA, Fuster V, Murray CJL, Roth GA. Global burden of cardiovascular diseases and risks, 1990−2022. *J Am Coll Cardiol* 2023;**82**:2350−473.
2. The WCOTROCHADIC. Report on cardiovascular health and diseases in China 2022: an updated summary. *Biomed Environ Sci* 2023;**36**:669−701.
3. Goldsborough 3rd E, Osuji N, Blaha MJ. Assessment of cardiovascular disease risk: a 2022 update. *Endocrinol Metab Clin N Am* 2022;**51**:483−509.
4. Duan HXY, Zhang Q, Liu J, Li RL, Wang D, Peng W, et al. Suppression of apoptosis in vascular endothelial cell, the promising way for natural medicines to treat atherosclerosis. *Pharmacol Res* 2021;**168**:105599.
5. Dri E, Lampas E, Lazaros G, Lazarou E, Theofilis P, Tsioufis C, et al. Inflammatory mediators of endothelial dysfunction. *Life* 2023;**13**:1420.
6. Wang M, Hao HF, Leeper NJ, Zhu LY, Early Career Committee. Thrombotic regulation from the endothelial cell perspectives. *Arterioscler Thromb Vasc Biol* 2018;**38**:e90−5.
7. Lippi G, Franchini M, Targher G. Arterial thrombus formation in cardiovascular disease. *Nat Rev Cardiol* 2011;**8**:502−12.
8. Poredoš P. Interrelationship between venous and arterial thrombosis. *Int Angiol* 2017;**36**:295−8.
9. Kleinegris MC, Ten Cate-Hoek AJ, Ten Cate H. Coagulation and the vessel wall in thrombosis and atherosclerosis. *Pol Arch Med Wewn* 2012;**122**:557−66.
10. Chamundeeswari M, Jeslin J, Verma ML. Nanocarriers for drug delivery applications. *Environ Chem Lett* 2019;**17**:849−65.
11. Tripathi S, Siddiqui MH, Kumar A, Vimal A. Nanoparticles: a promising vehicle for the delivery of therapeutic enzymes. *Int Nano Lett* 2023;**13**:209−21.
12. Andrews RK, Berndt MC. Platelet physiology and thrombosis. *Thromb Res* 2004;**114**:447−53.
13. Girolami A, Cosi E, Ferrari S, Lombardi AM, Girolami B. Prethrombotic, prothrombotic, thrombophilic states, hypercoagulable state, thrombophilia etc.: semantics should be respected even in medical papers. *J Thromb Thrombolysis* 2017;**43**:390−3.
14. Zhang YP, Ehrlich SM, Zhu C, Du XP. Signaling mechanisms of the platelet glycoprotein Ib-IX complex. *Platelets* 2022;**33**:823−32.
15. Delaney MK, Liu JL, Zheng Y, Berndt MC, Du XP. The role of Rac1 in glycoprotein Ib-IX-mediated signal transduction and integrin activation. *Arterioscler Thromb Vasc Biol* 2012;**32**:2761−8.
16. Chen YF, Ruggeri ZM, Du XP. 14−3−3 proteins in platelet biology and glycoprotein Ib-IX signaling. *Blood* 2018;**131**:2436−48.
17. Han HJ, Bártolo R, Li JC, Shahbazi M-A, Santos HA. Biomimetic platelet membrane-coated nanoparticles for targeted therapy. *Eur J Pharm Biopharm* 2022;**172**:1−15.
18. Wei XL, Ying M, Dehaini D, Su YY, Kroll AV, Zhou JR, et al. Nanoparticle functionalization with platelet membrane enables multifactored biological targeting and detection of atherosclerosis. *ACS Nano* 2018;**12**:109−16.
19. Wang SY, Duan Y, Zhang QZ, Komarla A, Gong H, Gao WW, et al. Drug targeting *via* platelet membrane−coated nanoparticles. *Small Struct* 2020;**1**:2000018.
20. Dong ZF, Tang L, Zhang Y, Ma XY, Yin Y, Kuang L, et al. A homing peptide modified neutrophil membrane biomimetic nanoparticles in response to ROS/inflammatory microenvironment for precise targeting treatment of ischemic stroke. *Adv Funct Mater* 2024;**34**:2309167.
21. Pan JM, Wang ZH, Huang XH, Xue J, Zhang SL, Guo X, et al. Bacteria-derived outer-membrane vesicles hitchhike neutrophils to enhance ischemic stroke therapy. *Adv Mater* 2023;**35**:2301779.
22. Gao C, Huang QX, Liu CH, Kwong CHT, Yue LD, Wan JB, et al. Treatment of atherosclerosis by macrophage-biomimetic nanoparticles *via* targeted pharmacotherapy and sequestration of pro-inflammatory cytokines. *Nat Commun* 2020;**11**:2622.
23. Cilia La Corte AL, Philippou H, Ariëns RA. Role of fibrin structure in thrombosis and vascular disease. *Adv Protein Chem Struct Biol* 2011;**83**:75−127.
24. Tsai YT, Zhou J, Weng H, Tang EN, Baker DW, Tang LP. Optical imaging of fibrin deposition to elucidate participation of mast cells in foreign body responses. *Biomaterials* 2014;**35**:2089−96.
25. Zhao ZQ, Zhang XB, Zhang HY, Shan XZ, Bai MY, Wang Z, et al. Elaborately engineering a self-indicating dual-drug nanoassembly for site-specific photothermal-potentiated thrombus penetration and thrombolysis. *Adv Sci (Weinh)* 2022;**9**:2104264.
26. Alonso-Alonso ML, Pérez-Mato M, Sampedro-Viana A, Correa-Paz C, Ávila-Gómez P, Sobrino T, et al. Fibrin-targeted nanoparticles for finding, visualizing and characterizing blood clots in acute ischemic stroke. *Pharmaceutics* 2022;**14**:2156.
27. Huang LJ, Zhang YJ, Zhao L, Chen QY, Li L. Ferrostatin-1 polarizes microglial cells toward M2 phenotype to alleviate inflammation after intracerebral hemorrhage. *Neurocritical Care* 2022;**36**:942−54.
28. Wang Y, Liu ZH, Li LY, Zhang ZY, Zhang K, Chu M, et al. Antiferroptosis exosomes engineered for targeting M2 microglia to improve neurological function in ischemic stroke. *J Nanobiotechnol* 2024;**22**:291.

29. Covarrubias A, Byles V, Horng T. ROS sets the stage for macrophage differentiation. *Cell Res* 2013;**23**:984−5.
30. Ma HT, Huang YT, Tian WR, Liu JC, Yan XY, Ma L, et al. Endothelial transferrin receptor 1 contributes to thrombogenesis through cascade ferroptosis. *Redox Biol* 2024;**70**:103041.
31. Yuan W, Xia H, Xu Y, Xu C, Chen N, Shao C, et al. The role of ferroptosis in endothelial cell dysfunction. *Cell Cycle* 2022;**21**:1897−914.
32. Gianopoulos I, Daskalopoulou SS. Macrophage profiling in atherosclerosis: understanding the unstable plaque. *Basic Res Cardiol* 2024; **119**:35−56.
33. Chinetti-Gbaguidi G, Colin S, Staels B. Macrophage subsets in atherosclerosis. *Nat Rev Cardiol* 2015;**12**:10−7.
34. Wen Q, Zhao HY, Lyu ZS, Weili Y, Han TT, Chen YH, et al. M1 and M2 macrophages play different roles in the pathogenesis of acute graft-versus-host disease post-allotransplant by modulating immune microenvironment. *Blood* 2020;**136**:19−20.
35. Lin L, Ba ZJ, Tian H, Qin HX, Chen X, Zhou X, et al. Ultrasound-responsive theranostic platform for the timely monitoring and efficient thrombolysis in thrombi of tPA resistance. *Nat Commun* 2024;**15**:6610.
36. Sun MJ, Liu C, Liu J, Wen J, Hao TJ, Chen DQ, et al. A microthrombus-driven fixed-point cleaved nanosystem for preventing post-thrombolysis recurrence *via* inhibiting ferroptosis. *J Control Release* 2024;**367**:587−603.
37. Förstermann U, Münzel T. Endothelial nitric oxide synthase in vascular disease: from marvel to menace. *Circulation* 2006;**113**:1708−14.
38. Wohlfart P, Xu H, Endlich A, Habermeier A, Closs EI, Hübschle T, et al. Antiatherosclerotic effects of small-molecular-weight compounds enhancing endothelial nitric-oxide synthase (eNOS) expression and preventing eNOS uncoupling. *J Pharmacol Exp Therapeut* 2008;**325**:370−9.
39. Ye W, Wang J, Little PJ, Zou J, Zheng Z, Lu J, et al. Anti-atherosclerotic effects and molecular targets of ginkgolide B from *Ginkgo biloba*. *Acta Pharm Sin B* 2024 Jan;**14**:1−19.